Solid State Phenomena
ISSN: 1662-9779, Vol. 390, pp 145-161
doi:10.4028/p-qnv3tQ

Submitted: 2026-01-19
Revised: 2026-02-18
Accepted: 2026-02-21
Online: 2026-04-17

Microscale to Macroscale Analyses of Superplasticity of Ti-6242S Titanium Alloy

AROWOLO Muritala[1,2,a*], VELAY Vincent.[2,b], VIDAL Vanessa[2,c] and DEHMAS Moukrane[1,d]

[1]CIRIMAT, Toulouse INP, Université de Toulouse, CNRS, Toulouse 31030, France

[2]Institut Clément Ader (ICA), Université de Toulouse, CNRS UMR 5312, IMT Mines Albi, INSA, ISAE-Supaéro, INSA, UPS, France

[a]muritala.arowolo@mines-albi.fr, [b]vincent.velay@mines-albi.fr, [c]vanessa.vidal@mines-albi.fr, [d]moukrane.dehmas@toulouse-inp.fr

Keywords: Multiscale modelling, CPFE, optimisation, HEXRD, dual-phase titanium alloy, superplasticity

Abstract. The superplastic performance of the dual-phase Ti-6242S titanium alloy makes it a good material for aerospace applications to produce structural components using the advanced superplastic forming (SPF) process. The need to optimize the SPF process demands the understanding and quantification of the influence of the different phase constituents - α and β on the global superplastic behaviour. Numerical modelling has been useful to predict mechanical behaviour for both a one-level and a multiscale approach. Multiscale approach: bottom-up (microscale to macroscale) has enabled understanding how the different microstructural parameters influence global material/structural mechanical response; which by and large means the modelling approach depends on the material local properties. The identification of these local properties is non-trivial in polycrystal materials, particularly at superplastic (elevated) temperatures.

Herein presented, is a new methodology that permits the quantification of the microstructural parameters of each of the constitutive phases of a polycrystal at a superplastic temperature using a genetic algorithm optimisation method on the data from in-situ high energy X-ray diffraction (synchrotron radiation), coupled with SEM (scanning electron microscope) and EBSD (electron backscattered diffraction). These identified local microstructural parameters were directly used in the finite strain crystal plasticity model to simulate the materials global response. This approach enabled the quantification of the phase influences on global behaviour with great accuracy.

It was found that α phase planes have high critical resolved shearing stress (CRSS) at 730°C which is similar to their behaviour at room temperatures, while β phase slip planes have low CRSS that encourage slip shearing at low stress. However, more applied load is partitioned in the β phase than in the α phase, despite the fact that the β phase fraction is about 15% at 730°C.

Introduction

Superplasticity refers to the ability of a material to undergo large strain deformation without necking (thinning) [1–3], often achieving elongation which can reach or exceed 1000% depending on the microstructure and the processing conditions. Superplasticity is said to occur if the strain rate sensitivity (m) is equal to or more than 0.3 [1], and this behaviour is found at high temperatures above 50% of the materials melting temperature and at very low strain rates (~10^{-4} s^{-1}). The aerospace industry has leveraged this inherent material property to produce complex, near-net-shaped titanium components in one-shot through a manufacturing method called the superplastic forming process (SPF).

Titanium alloys are widely used in aerospace applications due to their excellent specific strength and resistance to corrosion, fatigue and creep [4]. Based on their stabilizing allowing elements, they are categorized as: (a) α alloy with a hexagonal closed packed (HCP) crystallographic structure, is stabilized by Al, O, N, C, etc; (b) β alloy with a body center cubic (BCC) crystallographic structure

is stabilized by Mo, Cr, Ta, V, Fe, etc; and (c) α + β alloy containing both phases at room temperature, which contains the stabilizers of the two in relative ratios.

The superplastic behaviour of titanium alloys depends on various microstructural factors such as grain size and morphology, texture and anisotropy, phase volume fraction, phase interfacial interaction and their potential evolution during plastic deformation. In addition to the microstructural features, forming parameters such as temperature and strain rate can also control the flow behaviour (as strain hardening, flow softening or steady-state behaviour) and different mechanisms including dislocation gliding, grain boundary sliding, dynamic recrystallisation and dynamic recovery.

Finite-element (FE) modelling has become essential for predicting such complex interactions. There exist different material/structural modelling approaches. A one-level models consider a macroscale behaviour and treats the material as homogeneous, and a multiscale model where at least two levels are coupled, for instance, the microscale or the mesoscale is used to simulate the macroscale response of the structure using a scale transition rule or a homogenization method to bridge the different scales. Multiscale approach (microscale to macroscale) permits the numerical quantification of each phase's contributions to the global/macroscopic mechanical behaviour of a dual-phase system.

However, accurate microscale material parameters are difficult to identify for each phase. Their identification requires combined advanced experimentation techniques, particularly at elevated temperatures at which superplasticity is observed (900°C for Ti-6242S). Previous studies using Scanning Electron Microscopy (SEM) [5] and Electron Back-Scattered Diffraction (EBSD) [6] before/after deformation provide valuable information, but cannot determine real-time phase evolution, making parameter identification highly dependent on uncertain optimisation bounds. Kapoor et al. [7] presented an alternative approach, where virtual X-ray simulation was performed to reproduce the lattice strains obtained from *in situ* high-energy X-ray diffraction (HEXRD) while concurrently using the input of the virtual X-ray simulation for a crystal plasticity finite element simulation, in an attempt to fit the macroscopic stress vs strain curve of the material. The drawdown of Kapoor et al. [7] approach is that, it is a two-way method, which would be computationally expensive.

Consequently, in this work, a new methodology (one-way) is presented to identify phase properties with accuracy and use these calibrated properties to numerically simulate the macroscopic mechanical behaviour of a dual-phase (α + β) Ti-6Al-2Sn-4Zr-2Mo-0.12Si (Ti-6242S) alloy. It combines HEXRD, SEM and EBSD to identify phase-level mechanical parameters for the alloy. HEXRD (advanced experimental technique) permit to follow real-time evolution of the material phases during heat-treatment and mechanical deformation at temperatures. The volume fraction and the lattice strains of the different planes in both α and β phases are measured. Hence, the mechanical microstructural properties of each phase are obtained through the use of a genetic algorithm optimisation method applied on the lattice strains and the macroscopic stress-strain evolution given by the force and displacement recorded from the tensile test apparatus of the HEXRD set-up. Likewise, the SEM techniques allow for obtaining the microstructural images, the grain sizes, and the phase fraction of the two phases. Similarly, the EBSD helps identify grain orientations and grain sizes. These parameters are then implemented in a finite-strain crystal plasticity framework to simulate the macroscopic behaviour using a 3D representative volume element (RVE) which take into account the grain orientation and phase volume fraction.

Methodology

Numerical Framework. A finite strain formulation is appropriate to model the large deformation typical of the superplasticity forming process. A dual-phase material is considered; therefore, the subsequent equations hold separately for α and β phases including the slip laws for which a power law was used for both β (BCC) and α (HCP), following the formulations in [8–12].

Index and notation adopted: (i) = {α, β} phase, bold letters (**a**) refers to tensors, "⊗" is a tensor/dyadic product, while "." is a dot product and if otherwise not stated, it is a matrix

multiplication, s = 1,2,…,$N_s^{(i)}$ is the slip system in the phase (i) where $N_s^{(i)}$ is the total slip system number, $\vec{a}$ represents direction vector, ":" is a double contraction, and 'x' is a vector product.

In crystal plasticity, the decomposition of the deformation gradient ($\bar{\mathbf{F}}$) is adopted, which assumes the multiplication of the elastic deformation gradient ($\bar{\mathbf{F}}_\mathbf{e}$) and plastic deformation gradient ($\bar{\mathbf{F}}_\boldsymbol{p}$) and shown in Eq. 1

$$\bar{\mathbf{F}} = \bar{\mathbf{F}}_e^{(i)} \mathbf{F}_p^{(i)} \tag{1}$$

Where $\bar{\mathbf{F}}_e^{(i)}$ describes the reversible lattice deformation gradient of each phase due to the external load, in contrast, $\mathbf{F}_p^{(i)}$ describes the irreversible deformation gradient of the lattice in each phase due to plastic work, which can be a convolution of rate-dependent and rate-independent plastic work, depending on the mechanisms intended to be captured. It also has to satisfy the incompressibility constraint (det $\mathbf{F}_p^{(i)}$ = 1) enforced with $\left(\mathbf{F}_p^{(i)}(\det \mathbf{F}_p^{(i)})^{\frac{-1}{3}}\right)$. The plastic velocity gradient ($\mathbf{L}_p^{(i)}$) is described as in Eq. 2:

$$\mathbf{L}_p^{(i)} = \dot{\bar{\mathbf{F}}}_p^{(i)} \bar{\mathbf{F}}_p^{(i)^{-1}} = \sum_{s=1}^{N_s^{(i)}} \dot{\gamma}_s^{(i)} \vec{m}_s^{(i)} \otimes \vec{n}_s^{(i)} \tag{2}$$

Where $\mathbf{L}_p^{(i)}$ relates the rate of plastic deformation gradient $\dot{\bar{\mathbf{F}}}_p^{(i)}$ to its inverse $\bar{\mathbf{F}}_p^{(i)^{-1}}$. $\mathbf{L}_p^{(i)}$ is related to the summation of shear strain rate $\dot{\gamma}_s^{(i)}$ on all the slip system of corresponding phase (i) with their corresponding Schmid factors described by the dyadic product of the slip direction $\vec{m}_s^{(i)}$ and the slip-plane normal $\vec{n}_s^{(i)}$. The shear strain rate $\dot{\gamma}_s^{(i)}$ is described by viscoplastic power laws for α and β phase as in Eq. 3:

$$\text{(i)} = \{\alpha, \beta\}: \qquad \dot{\gamma}_s^{(i)} = \dot{\gamma}_0^{(i)} \left(\frac{\tau_s^{(i)}}{\mathbf{g}_s^{(i)}}\right)^{n(i)} sign\left(\mathbf{Z}_s^{(i)}\right) \quad \text{if } \left|\tau_s^{(i)}\right| \geq \mathrm{g}_s^{(i)} \tag{3}$$

Where $\dot{\gamma}_0^{(i)}$ is the initial strain rate, $\tau_s^{(i)}$ is the resolved stress in each slip system (s), likewise $\mathrm{g}_s^{(i)}$is the critical resolved stress, $n(i)$ is the phase strain rate sensitivity. The resolved stress can be described as in Eq. 4 where $\boldsymbol{\sigma}^{(i)}$ is Cauchy stress:

$$\tau_s^{(i)} = \boldsymbol{\sigma}^{(i)} \mathbf{:} \vec{m}_s^{(i)} \otimes \vec{n}_s^{(i)} \tag{4}$$

The critical resolved stress $\mathrm{g}_s^{(i)}$ for both α and β shown in Eq. 5a depends on the initial resolved stress $\tau_0^{(i)}$ and evolution hardening function described as Eq. 5b:

$$\text{(i)} = \{\alpha, \beta\}: \ \mathrm{g}_s^{(i)} = \tau_0^{(i)} + \sum_{k=1}^{N_s^{(i)}} \mathrm{H}_{sk}^{(i)} \dot{h}_k^{(i)} \tag{5a}$$

$$\dot{h}_k^{(i)} = h_0^{(i)} \left(1 - \frac{\mathrm{g}_s^{(i)}}{\tau_{sat}^{(i)}}\right)^{m(i)} \left|\dot{\gamma}_s^{(i)}\right| \tag{5b}$$

The $\tau_{sat}^{(i)}$ is the saturated stress, $\mathrm{H}_{sk}^{(i)}$ is the phase slip hardening interaction matrix describing self-strain hardening ($\mathrm{H}_{kk}^{(i)}$ = 1) and latent hardening ($\mathrm{H}_{sk}^{(i)}$ = 1.4), $h_0^{(i)}$ is the initial hardening rate, $\mathrm{m}^{(i)}$ is the hardening exponent.

The constitutive law, which relates the strain and stress evolution in each phase is formulated in terms of an objective stress (rotation free). It is expressed using the Hill and Rice form of the Jaumann stress rate (σ_e^{∇}) as shown in Eq. 6 which can be written in terms of the symmetric and asymmetric parts of the Schmid tensor as shown in [13], see [9, 11] for details.

$$\sigma_e^{\nabla} + \boldsymbol{\sigma}\, \mathrm{tr}(\boldsymbol{De}) = \boldsymbol{C^g} : \boldsymbol{De} \tag{6}$$

Where $\boldsymbol{De}$, tr($\boldsymbol{De}$), is the elastic strain and its trace respectively; $\boldsymbol{C^g}$ is the fourth order grain stiffness matrix in the global coordinate shown in Eq. 7, obtained by rotating its local stiffness matrix

($\boldsymbol{C^l}$) with rotation matrix (**R**) formed with the grain Euler angles (θ, ψ, Φ) obtained from EBSD (electron backscattered diffraction)

$$C^g = [\mathbf{R} \otimes \mathbf{R}] : \boldsymbol{C^l} : [\mathbf{R^T} \otimes \mathbf{R^T}] \quad (7)$$

The above model formulation was implemented in Abaqus user material (UMAT) using the work of Eralp et al. [9]. The rule of mixture (Eq. 8) as a homogenization technique, was employed to obtain the global/macroscopic stress in the material, which depends on the volume fraction of α - f_α and the volume fraction of β - f_β

$$\sigma^g = f_\alpha \sigma^\alpha + f_\beta \sigma^\beta \quad (8)$$

Phase Material Properties Identification: Genetic Algorithm Optimisation. From the model formulation, various microstructural parameters for both α and β phase are necessary to realize the microscale to macroscale (bottom - up) numerical simulation. These include the single elastic constants (C_{11}^α, C_{33}^α, C_{12}^α, C_{13}^α, C_{44}^α, C_{11}^β, C_{12}^β, C_{44}^β); viscous and hardening parameters ($\tau_0^{(\alpha)}$, $\dot{\gamma}_0^{(\alpha)}$, $h_0^{(\alpha)}$, $\tau_{sat}^{(\alpha)}$, m(α), $n(\alpha)$, $\tau_0^{(\beta)}$, $\dot{\gamma}_0^{(\beta)}$, $h_0^{(\beta)}$, $\tau_{sat}^{(\beta)}$, m(β), $n(\beta)$).

The single elastic constants of the different phases were identified from in-situ HEXRD lattice strain measurements by reconstructing micro-strain tensors of each phase, applying micromechanical homogenization to compute macroscopic stress, and solving an inverse optimisation problem using a genetic algorithm under elastic stability constraints [14, 15]. The parameters were obtained by minimizing the discrepancy between the computed macroscopic stress and the experimental uniaxial stress in the elastic domain.

To identify the visco-plastic parameters of the two phases, the micro-strain evolution for the relevant crystallographic planes of α and β phases (derived in the section of Phase Micro-strain Lattice Determination below) was used as input for a genetic algorithm optimisation. This was possible with the assumption that, for the respective {hkl} planes in each phase, its micro-strain tensors are equivalent to its elasto-viscoplastic strain, and these cumulatively resolved to the global elasto-viscoplastic strain in each of the phases.

For instance, in β phase, micro-strain tensors associated with {110} and {200} planes are considered to govern the global elasto-viscoplastic behaviour in β phase, while α phase micro-strain computed on basal {0002}, prismatic $\{10\bar{1}0\}$, $\{11\bar{2}0\}$; and pyramidal $\{10\bar{1}1\}$, $\{10\bar{1}2\}$ planes cumulatively govern to the α phase elasto-viscoplastic behaviour. To formulate the optimisation problem, an equivalent elasto-viscoplastic strain was computed for each {hkl} plane using the von Mises strain definition (Eq. 9a), based on the {hkl} strain tensors presented in the section of Phase Micro-strain Lattice Determination below**.**

$$\varepsilon_{vm}^{hkl} = \sqrt{\frac{2}{3}(\boldsymbol{\varepsilon}^{hkl} : \boldsymbol{\varepsilon}^{hkl})} \quad (9a)$$

These equivalent micro-strain evolutions served as the target data for the genetic algorithm fitting procedure such as (Eq. 9b):

$$(i) = \{\alpha, \beta\}: \ \gamma_s^{hkl\,(i)} = \varepsilon_{vm}^{hkl} \quad (9b)$$

The optimisation objective functions - which are visoplastic slip functions Eqs. 3, 5a and 5b, were defined to identify the visco-plastic parameters for each {hkl} in both α and β phase ($\tau_0^{(\alpha)}$, $\dot{\gamma}_0^{(\alpha)}$, $h_0^{(\alpha)}$, $\tau_{sat}^{(\alpha)}$, m(α), $n(\alpha)$, $\tau_0^{(\beta)}$, $\dot{\gamma}_0^{(\beta)}$, $h_0^{(\beta)}$, $\tau_{sat}^{(\beta)}$, m(β), $n(\beta)$). The shear strain equation was solved using Newton Raphson algorithm and it was included in the genetic algorithm, where the bounds (upper and lower) was reasonably defined for each of the parameters. The macroscopic uniaxial stress (σ_{11}) obtained from the uniaxial experiment was factored by a factor (M) defined as 1.35 (to account for the applied stress and slip plane direction) as shown in Eq. 10, and was used as the resolved stress. It

served as the forcing function in the optimization algorithm at each corresponding shearing strain increment.

$$\sigma_{vm}^{g} = \mathrm{M}\,\sigma_{11} \tag{10}$$

The quality of the fit was evaluated using the root mean square error (RMSE) calculated using Eq. 11, where N is the total population reasonably defined to minimize the computation time.

$$\mathrm{RMSE} = \sqrt{\frac{1}{N}\sum_{i=1}^{N}(x_i - x_j)^2} \tag{11}$$

where $x_i, x_j, \ldots, x_N$ is each of the computed values for an optimized parameter in the population.

It should be noted that $\mathrm{H}_{sk}^{(i)}$, the hardening interaction coefficient was assumed to be 1.0 in the optimisation solution. The softening beyond global-yielding of the macroscopic stress-strain is not discussed here, as such, the ε_{vm}^{hkl} and σ_{vm}^{g} up to the 0.2 macroscopic true-strain was used for the fitting (to ensure that micro-strain up to saturation is considered).

Experimental Details. The real-time microstructural evolution was followed during a uniaxial tensile test performed at 730°C on a dual-phase (α + β) Ti-6Al-2Sn-4Zr-2Mo-0.12Si (Ti-6242S) alloy using a modified DIL 805 A/D deformation dilatometer (TA instruments) working at the P07 beamline of the Petra III, DESY, Hamburg, Germany.

Fig. 1a shows the 4mm thick dog-bone shaped sample machined from a 4mm thick plate, whose as-mounted schematic in the tensile apparatus of the thermomechanical simulator (DIL 805, TA instruments) is shown in Fig. 1b. A type-S thermocouple was welded at the surface in the mid-length of the sample to real-time control the sample temperature with a numerical regulator. The whole experiment was performed under secondary vacuum in order to prevent exposure to oxygen, which can cause α-case and can affect the ductility of the material.

Thanks to a high energy of 100 keV (λ of 0.124 $\dot{A}$), a large volume was analyzed by transmission of X-rays through 4 mm wide samples. Consequently, a 2D-dectector Perkin Elmer XRD 1621 Flat Panel with a resolution of 2048 by 2048 pixels was placed in transmission to collect the Debye-Scherrer ring. X-ray diffraction images were taken at intervals (acquisition rate of 0.2 Hz - 1 in every 5 s), which follows the complete test evolution during thermo-mechanical loading.

The experiment consisted of heating from room temperature up to the target temperature (730°C), followed by 10 mins holding time prior the mechanical loading, applied at the strain rate of 2 x 10^{-3} s^{-1}. The sample was not loaded to failure but to the maximum displacement limit of the equipment of 9 mm. Finally, rapid cooling was performed using argon gas at the rate of 140°C.s^{-1}.

The microstructural and the crystallographic details in both undeformed and post-deformed states were examined under SEM respectively, and EBSD was performed on the undeformed state. The critically deformed section of the sample, likewise, the initial state was cut and prepared with standard metallography technique without etching and observed under SEM in the back-scattered electron (BSE) mode with FEI NOVA nano SEM 450 equipment. While the EBSD was performed on the initial state sample, with OXFORD Instruments symmetry equipment with an accelerating voltage of 20 kV at a rate of 153.52 Hz.

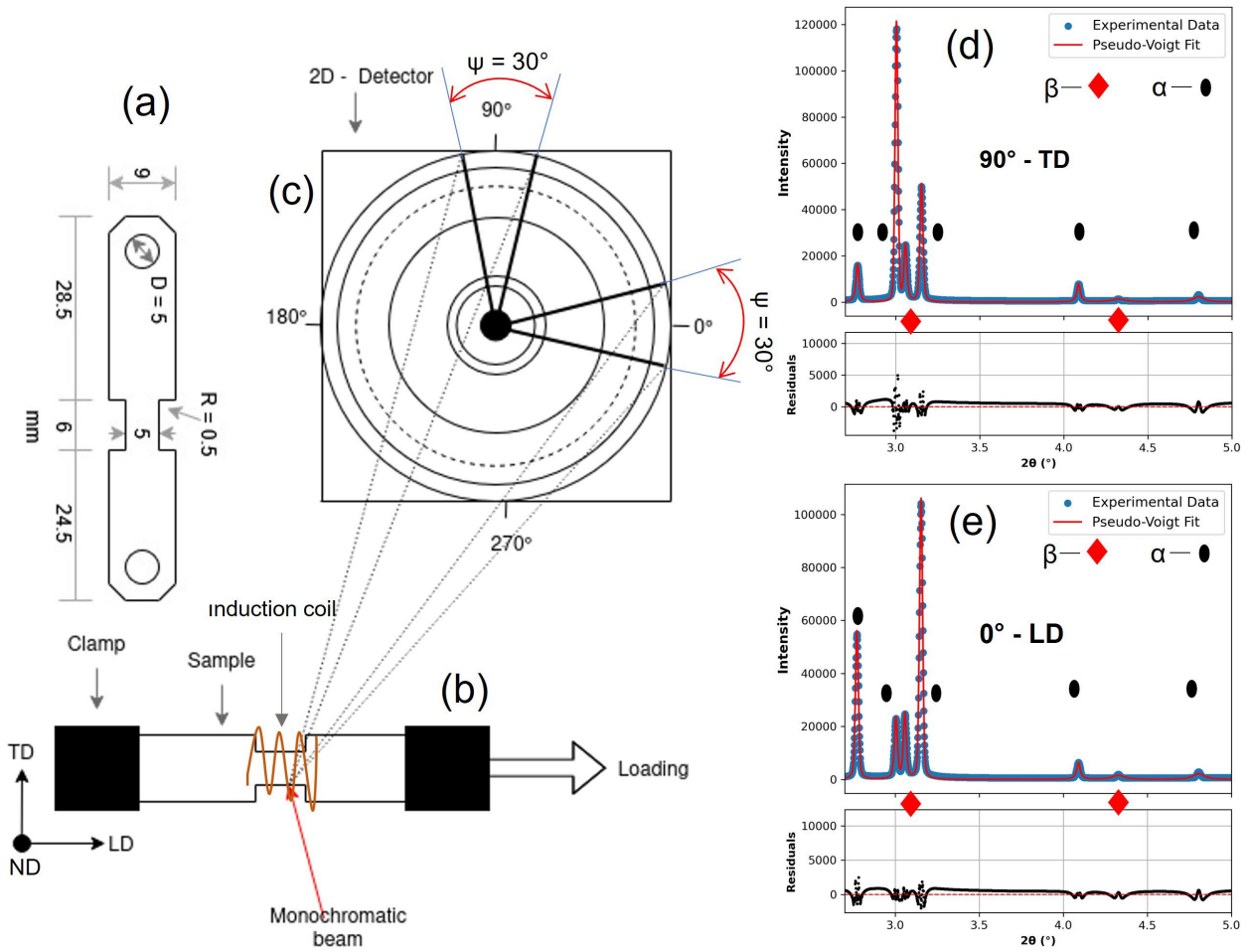

Fig.1. Schematic of in-situ uniaxial tensile test under synchrotron X-ray observation. Sample geometry (a); sample in clamped position in relation to X-ray beam source (b); 2D-dectector (c); typical result of partial integration of X-ray pattern about 90° - TD (d) and typical result of partial integration of X-ray pattern about 0° - LD (e).

Phase Micro-strain Lattice Determination. Based on the X-ray diffraction patterns recorded throughout the tensile test in temperature, the phase volume fraction and the mean lattice parameters of each phase were determined by using the Rietveld refinement method [16] on the 1D patterns, meaning by integrating fully around the azimuth of Debye-Scherrer rings.

In addition, partial integration of the X-ray diffraction patterns was performed to highlight the expected expansion along the loading direction and compression in the transverse direction. An azimuth angle (ψ) of 30° (±15°) about the orthogonal axes (Fig. 1c), together with its symmetric counterpart, was selected to ensure sufficient grain statistics. The partial integrations were performed using the pyFAI module developed by the European Synchrotron Radiation Facility [17]. Curve fitting of the experimental data was performed using Pseudo-Voigt function from the LMFIT Python library [18]. Typical fitting results along the sample transverse and the loading direction are shown in Figs. 1d and 1e.

From these fitted diffraction data obtained for the two-perpendicular directions, the d-spacing d^{hkl} was determined using Bragg's law [19]. The corresponding elastic lattice micro-strain for each {hkl} plane in both phases was then calculated using Eq. 12a. Here, d_0^{hkl} denotes the reference d-spacing of the {hkl} plane, taken as the {hkl} d-spacing before the mechanical loading was applied.

$$\varepsilon^{hkl} = \frac{d^{hkl} - d_0^{hkl}}{d_0^{hkl}} \tag{12a}$$

Considering that the X-ray monochromatic beam is incident on the sample at a diffraction angle 2θ, the effect of beam geometry was normalized by averaging of the micro-strain ε^{hkl} obtained from Eq. 12a at azimuthal angles 0° and 180°, defining the loading direction strain ε_{LD}^{hkl}. Similarly, averaging the values obtained at 90° and 270° yields the transverse direction strain ε_{TD}^{hkl}, as expressed in Eq. 12b. The normal direction (ND) is the 3rd orthogonal axes along the thickness of the sample (as shown in Fig. 1). Since the experiment involves uniaxial loading, a transversely isotropic behaviour can be assumed. Consequently, the transverse and normal micro-strains are considered equal due to the Poisson effect such that $\varepsilon_{TD}^{hkl} = \varepsilon_{ND}^{hkl}$, implying $\varepsilon_{22}^{hkl} = \varepsilon_{33}^{hkl}$. Under these assumptions, all the diagonal of the ε_{ij}^{hkl} strain tensor for each {hkl} plan (a second-order tensor where i,j = 1,2,3 representing the three orthogonal reference coordinates) (Eq. 12c) can be determined while the off diagonal strains are assumed to be null.

$$\varepsilon_{LD}^{hkl} = \frac{\varepsilon_{0°}^{hkl} + \varepsilon_{180°}^{hkl}}{2} \; ; \; \varepsilon_{TD}^{hkl} = \frac{\varepsilon_{90°}^{hkl} + \varepsilon_{270°}^{hkl}}{2} \tag{12b}$$

$$\boldsymbol{\varepsilon_{ij}^{hkl}} = \begin{pmatrix} \varepsilon_{LD}^{hkl} & 0 & 0 \\ 0 & \varepsilon_{TD}^{hkl} & 0 \\ 0 & 0 & \varepsilon_{TD}^{hkl} \end{pmatrix} \tag{12c}$$

Microstructure Generation and Modelling Approach. A RVE of 1 x 1 x 1 μm^3 with 100 grains was generated with Neper [20] to replicate the material microstructure. The grain orientations obtained from EBSD analyses were incorporated into the RVE generation to ensure that they approximatively represent the same grain orientation distribution as the actual material. Neper was also used for the meshing, using C3D8 elements with a size of 0.05 μm, which is lower than the average grain size (2.3 μm) in order to eliminate mesh dependency and sensitivity (see Fig. 2a).

In order to account for the phase volume fractions, the group option was used in Neper which permits specifying the number of different grains for α and β phases, to represent their volume fraction (f_α - 85% and f_β – 15% at 730°C determined from Rietveld refinement). The grains for each phase are shown in Fig. 2a, and the assembly is shown in Fig. 2b. Each group was assigned a distinct identifier (1 for α phase and 2 for β phase) to differentiate the phases. In the input file generated for Abaqus, two element set instances were created at the assembly level to group the grains according to the identifiers. This approach allowed assigning different material properties to the grains based on their respective phases.

Boundary conditions were applied to the RVE: symmetry conditions were used to constrain rotation about, and deformation along, the -X, -Y, and -Z axes, while a displacement corresponding to 0.20 true strain (22.14% engineering strain) was applied on the X-face of the RVE in the X direction to replicate the uniaxial displacement imposed on the macroscopic sample (Fig. 2c).

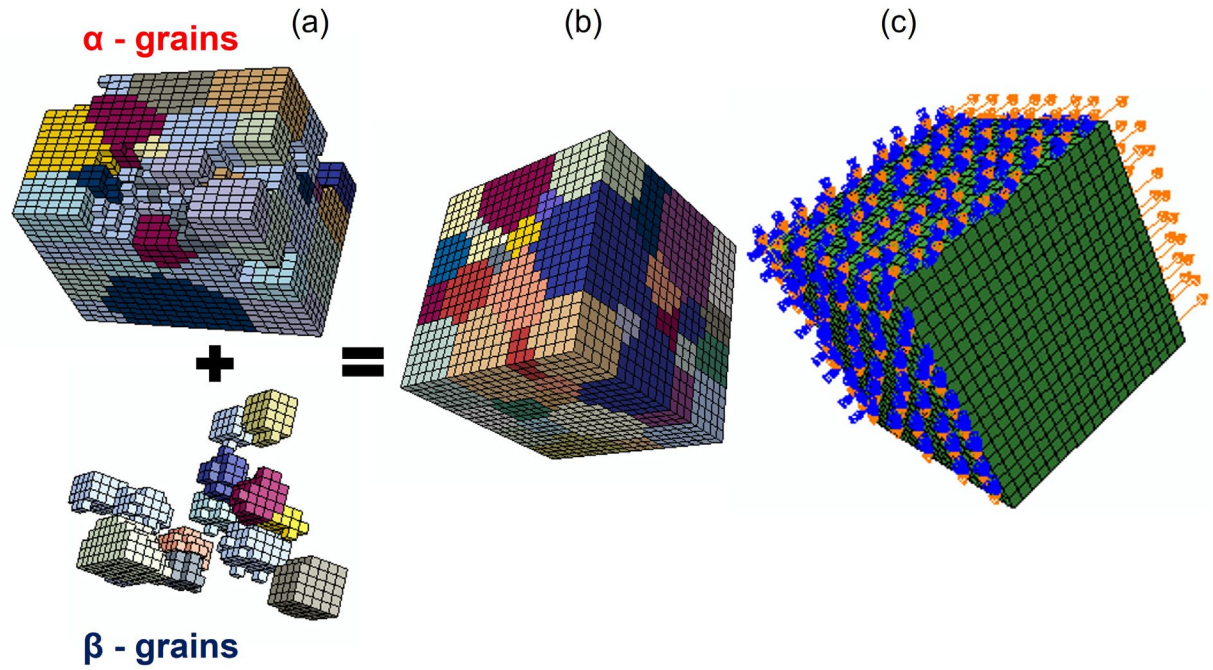

Fig. 2. Images of Representative volume elements (RVE). Representation of α and β grains (a); Assembly of α and β grains with global mesh view (b); and boundary conditions descriptions (c).

Results and Discussion

As mentioned above, the microscale to macroscale numerical modelling approach adopted herein depends on advanced experimental techniques; as such, both results of experiments and numerical modelling are presented chronologically.

Microstructure and Mechanical Behaviour. Figs. 3a and 3b respectively show the BSE-SEM micrograph and the inverse pole figure at the as-received state of Ti-6242 titanium alloy. The microstructure consists of nodular α phase surrounded by a β phase network. The β phase appears with a lighter contrast, and the α phase exhibits a darker contrast. The mean equivalent diameter of the α nodules is found to be approximately 2.3 μm. From image analysis, the β volume fraction is about 10 % at room temperature, which is consistent with the value obtained by Rietveld refinement of the diffraction pattern and similar to the value reported by Kapoor et al. [19].

Fig. 3c displays a true stress - true strain curve obtained at 730°C and a strain rate of 2.10^{-3} s^{-1}. Three distinct stages can be identified: i) a small elastic domain followed by, ii) a plastic deformation region characterized by strain hardening up to the ultimate stress, and iii) a subsequent flow softening regime. The latter is not discussed here, as beyond a true strain of about 0.54, the temperature is no longer constant at 730°C. The sharp transition from elastic to plastic at strain of about 0.001 (Fig. 3d) can easily go unnoticed. Beyond that, the observed hardening and subsequent softening behaviour are consistent with previously reported results for the same alloy and Ti-6Al-4V alloy at temperatures around 700°C [5, 6, 21, 22].

The microstructure at the critically deformed section is shown in Fig. 3e. Both the α and β grains became more elongated along the RD, which coincides with the loading direction, and the β phase fraction has increased to approximate 15% (Rietveld refinement). In addition, micro-voids (black spots) are observed, predominantly within the β phase and at the α/β interfaces. The porosities had been similarly reported for Ti-6Al-4V and Ti-6242S alloys at superplastic temperatures [5, 6], with the extent of porosity strongly dependent on strain rate and temperature.

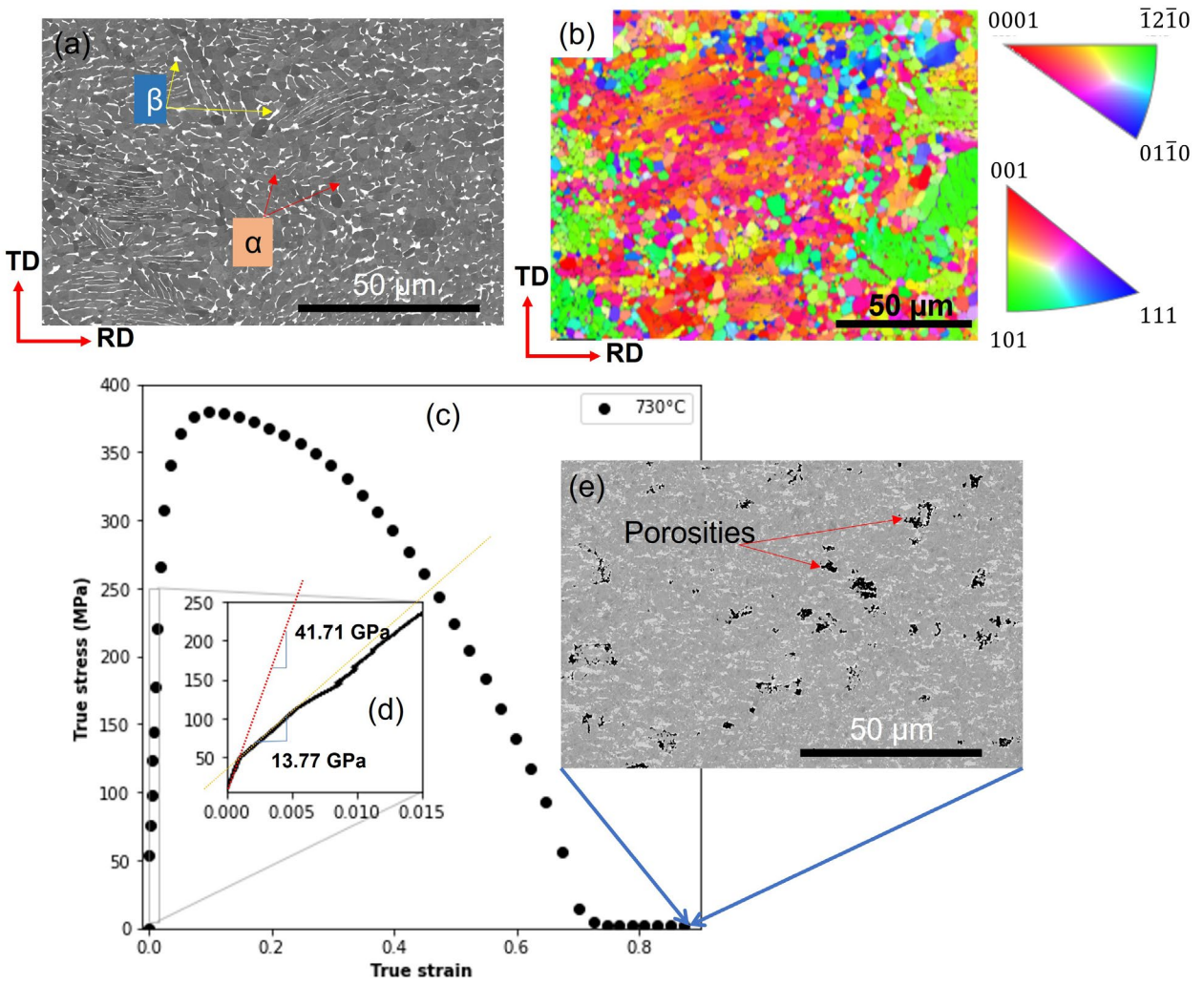

Fig. 3. BSE-SEM micrograph at the as-received state of Ti-6242 titanium alloy (a); inverse pole figure of the as-received state (b); true stress - true strain curve (c); magnified zone of on-set of local plastic transition zone (d); and BSE-SEM micrograph of test sample post mechanical deformation at 730°C (e).

Microstructural Behaviour Under Mechanical Loading at 730°C. To understand the respective contributions of the α and β phases to the macroscopic mechanical behaviour described in (Microstructure and Mechanical Behaviour, see Fig. 3c), the strain-induced evolution of each phase is investigated and presented using two complementary approaches. First, the 1D profiles of the HEXRD patterns are analyzed to assess the global response of each phase. Second, partial integration of the HEXRD patterns is performed to quantify the phase-specific response to loading along both the LD and TD direction. These results are subsequently used to identify the microstructural parameters required for the finite strain CPFE modelling.

Qualitative Evolution – 1D profiles. Fig. 4a presents the 1D profiles of the HEXRD patterns, illustrating the global evolution of phases within the microstructure throughout mechanical loading, and Fig. 4b shows a magnified region of the 1D profiles between 5.4° and 5.9°. The peaks corresponding to the α and β phases are indexed as indicated in Fig. 4. As shown in Fig. 4b, increasing macroscopic true strain leads to a systematic shift of the diffraction peaks toward lower diffraction angles for both phases, which reflects an increase in elastic lattice micro-strain within the different crystallographic planes.

In addition, the shape of the α peaks in the 2θ range of 5.4° - 5.9° becomes asymmetric (can be slightly observed in lower angles), which increases up to a true strain of 0.6 (equivalent of 82 % in engineering strain). The loss of the peaks asymmetric shape at true strain above 0.7 can be linked to the rise in

temperature above 730°C earlier mentioned. This asymmetry of the peaks is an indication of anisotropic strain behaviour in the α phase under mechanical loading, which can likely be caused by grain size heterogeneity [23–25]. Peak asymmetry may also arise from the combined effects of crystallite size heterogeneity and chemical heterogeneity. However, the latter can be excluded in the present case, as the microstructure is close to thermodynamic equilibrium. In addition, it can be noticed that the pronounced asymmetry observed for the pyramidal planes of α phase - $\{11\bar{2}2\}$, $\{20\bar{2}1\}$ and can be attributed to the higher sensitivity of these crystallographic orientations to anisotropic lattice strain and heterogeneous deformation under applied loading.

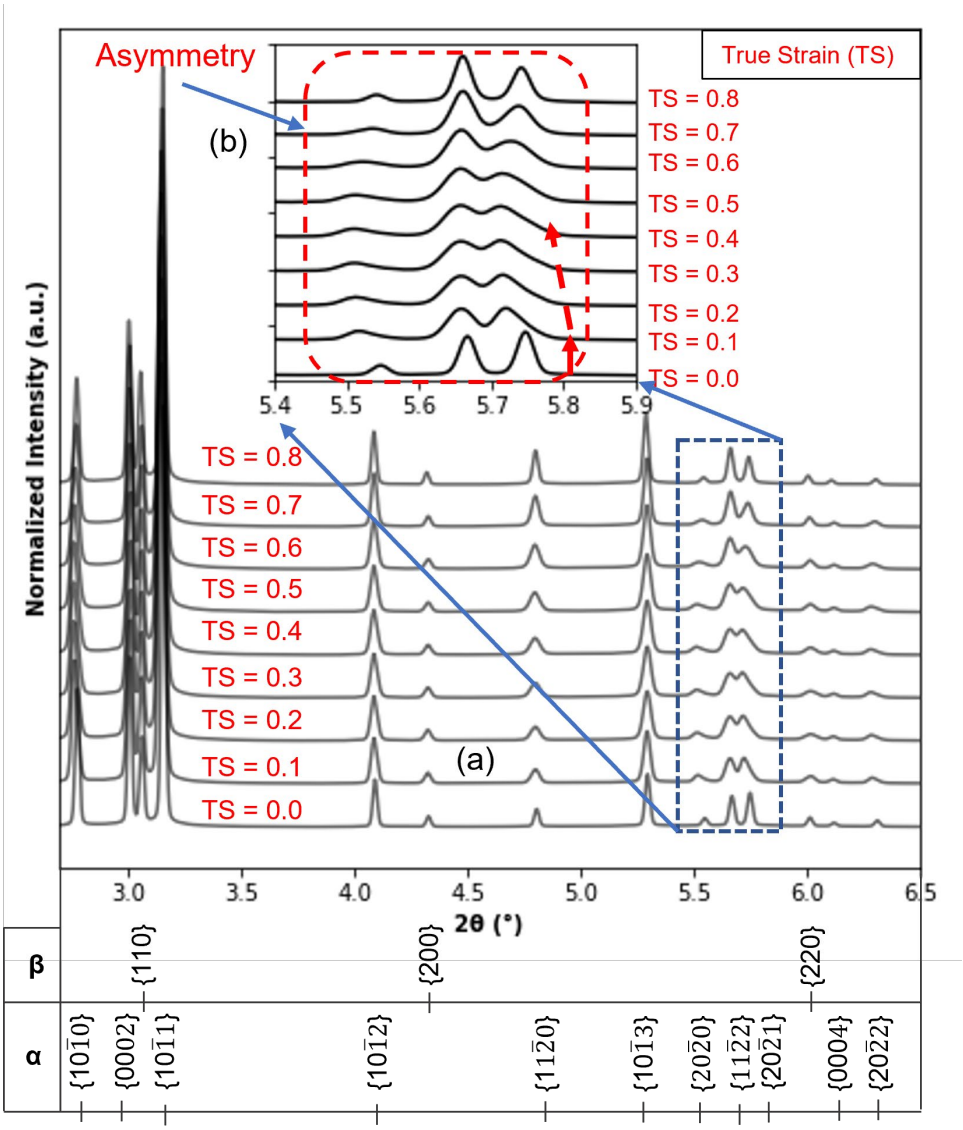

Fig. 4. Evolution of 1D profiles during mechanical loading at 730°C in the range between 2.7° - 6.5° (a); and in the range between 5.4° - 5.9° to highlight the asymmetry peaks of α phase (b).

Equivalent Lattice Strain Evolution – 2D profiles. Using the partial integration method, the result of the elastic micro-strain evolution of the different crystallographic planes of both α and β phases along LD and TD are reported in Figs 5a and 5b, respectively. The following crystallographic planes are examined for the α phase: basal - {0002} planes, prismatic - $\{10\bar{1}0\}$ planes, $\{11\bar{2}0\}$, and pyramidal - $\{10\bar{1}1\}$, $\{10\bar{1}2\}$ planes, while {110} and {200} planes are considered for the β phase.

The different $\{hkil\}_\alpha$ planes exhibit distinct responses, as evidenced by the varying stiffening/hardening rates observed among them, particularly along the loading direction. Note that these different evolutions of the selected lattice strain ε^{hkl}, in particular at low true strain, tend to

reflect the elastic anisotropy of the α phase. Indeed, in accordance with trends reported in [26, 27], the $\{10\bar{1}0\}$ plane have a more compliant behaviour compared to the $\{10\bar{1}1\}$, and the {0002} planes. In contrast, the two $\{110\}_\beta$ and $\{200\}_\beta$ planes show similar behaviour, which reached a plateau at a very low lattice strain and evolved closely as the macroscopic true strain increases. This trend indicates that strain accommodation is mainly governed by the α phase, especially by the prismatic $\{10\bar{1}0\}$ planes. The behaviour is in contrast with reports for the same Ti-6242S alloy and for Ti-64 alloy [19], likewise [28] for Ti-Al-V-Fe-Si-O a (α + β) titanium alloy. These contrastive behaviours can be directly linked to the temperature effect. Furthermore, Figs. 5a and 5b clearly reveal the Poisson effect in both $\{hkil\}_\alpha$ and $\{hkl\}_\beta$ planes: most $\{hkil\}_\alpha$ planes attain a plateau rapidly at low strain, except for the basal plane, which continues to exhibit an increase in the lattice strain.

The correlation of the first deviation of the flow stress obtained from experiment from elasticity at the small strain in Fig. 5c and the different inflection/deviation of the lattice strains in the different planes can be linked to the local onset of plasticity and also to changes in load distribution between different grains (with different orientation) and/or phases. In addition, Fig. 5d shows the lattice strains evolution with the macroscopic true stress. The different planes of both α and β planes behaved linearly (approximately) at different stress range, upon which a change or deflection of the linear evolution is observed, which signaled yielding. The crystallographic planes of the β phase yield at much lower stress compared to those of the α phase planes.

Since the objective is to identify microscale parameters for numerical modelling as stated earlier, it is necessary to establish a link between the observed lattice strains in each phase ($\{hkil\}_\alpha$ and $\{hkl\}_\beta$) and the corresponding phase-level strain response. As previously stated, it was assumed that the elasto-viscoplastic strain experienced in each phase results from the cumulative contribution of lattice strains associated with the different crystallographic planes of the phase. Accordingly, the phase lattice strains shown in Fig. 5a, calculated using Eq. 12a, were used to construct strain tensors as defined in Eq. 12c. The strain von Mises (Eq. 9a) was then applied to these phase lattice strain tensors to obtain the equivalent lattice strain of each phase.

The resulting equivalent phase lattice strains are presented as scattered data points in Fig. 5c. This equivalent phase lattice strain was further simulated using the hardening laws earlier presented in the numerical framework above, while attempting to optimize the material parameters that describes the strain evolution. The optimized elasto-viscoplastic strain functions for the different $\{hkil\}_\alpha$ and $\{hkl\}_\beta$ planes are shown as continuous lines in Fig. 5c. It is interesting to recognize that the equivalent phase lattice strains and their optimized fits follow the same trend reported for the phase lattice strain (Fig. 5a), thereby showing the consistency of the proposed microstructural phase properties identification method.

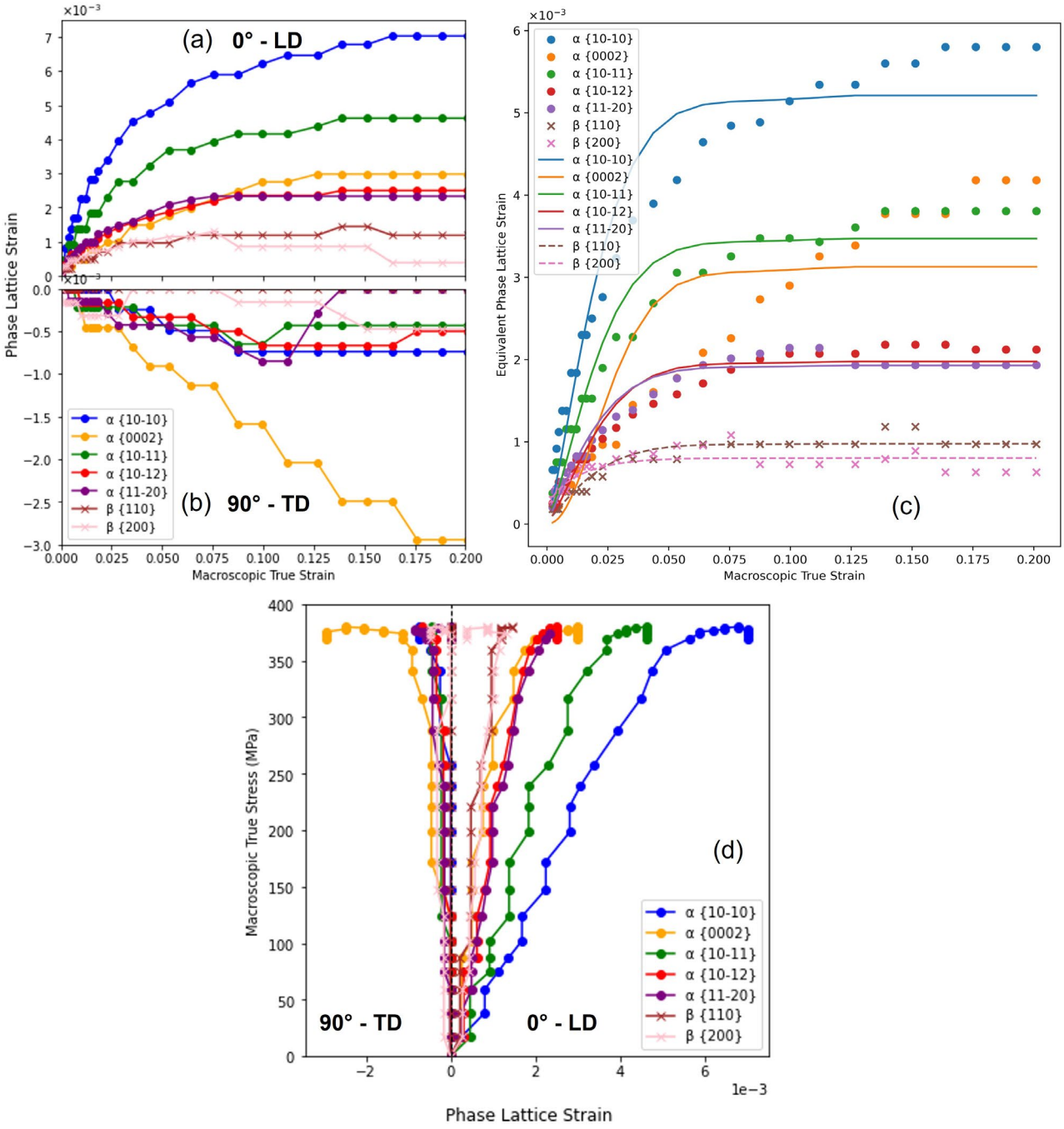

Fig. 5. Phase micro-strain evolution. Micro-strains in loading direction vs macroscopic strain (a), micro-strains in transverse direction vs macroscopic strain (b); von Mises equivalent of phase micro-strain vs macroscopic strain (c); and phase micro-strain evolution with macroscopic true stress (d).

Numerical Model Result. The simulation was performed on was performed with 12 BCC crystallographic system – $\{110\}\langle 111\rangle$ and 12 HCP crystallographic system – 3 Basal $\{0001\}\langle 11\bar{2}0\rangle$, 3 prismatic $\{10\bar{1}0\}\langle 11\bar{2}0\rangle$, and 6 pyramidal $\{10\bar{1}1\}\langle 11\bar{2}0\rangle$. The optimisation search range (upper and lower bound) is reported in table 1 and the result of the optimized parameters for both the $\{hkil\}_\alpha$ and $\{hkl\}_\beta$ are listed in table 2, which resulted in the simulated result (continuous line) reported in fig 5c. It is necessary to note that the behaviour of Basal $\{0002\}$ equivalent lattice strain is linear up to saturation, as such, the shearing equation (Eq. 3) used for the fitting could not reproduce it well. As such, the values calibrated for prismatic $\{10\bar{1}1\}$ was adopted for Basal slip system in the simulation because the two seems to have yielded and saturated closely (Figs. 5a and c).

It is necessary to mention that the authors are not oblivious of the need for uniqueness of the identified material parameters in order to be able to predict the material response under varying strain rates; however, this prove of concept has only been tested for experiment under a single strain rate of 2 x 10^{-3}. Although the uniqueness has been judged by the fitness of the fit considered within different optimisation search bounds. However, further analyses would be performed using data from different strain rates in future study.

The calibrated values of the initial critical shear stress (τ_0) for HCP slip planes at 730°C reported here is in the same range of values reported by Séchepée et al. [29] for the same material (Ti-6242S) with a f_β of 13%. Table 3 shows the values used for the finite crystal plasticity simulation, the results reported for $\{hkl\}_\beta$ - {110} was used as input for β phase, while the average of the calibrated parameters (Table 2) for for α phase planes ($\{10\bar{1}0\}$, {0002}, and $\{10\bar{1}1\}$) except for the initial resolved stress (τ_0), which the respective $\{hkil\}_\alpha$ values - basal - {0002}, prismatic - $\{10\bar{1}0\}$, and pyramidal - $\{10\bar{1}1\}$ were adopted for the simulation. Table 4 shows the summary of the single elastic constants at 730°C for both α and β phases used in the CPFE simulation.

Table 1. Optimisation search bounds.

	α	β
τ_0 [MPa]	150 - 430	40 - 100
γ_0 $[s^{-1}]$ (10^{-3})	10^{-4} - 10^{-2}	10^{-4} - 10^{-2}
h_0 [MPa]	20 - 400	10 - 50
τ_{sat} (MPa)	120 - 500	85 - 150
m	0.1 - 25	0.1 - 5
n	0.1 – 2.9	0.1 – 0.9

Table 2. Optimized microstructural model parameters for different crystallographic planes in α and β phase.

	α					β	
	$\{10\bar{1}0\}$	{0002}	$\{10\bar{1}1\}$	$\{10\bar{1}2\}$	$\{11\bar{2}0\}$	{110}	{200}
τ_0 [MPa]	425	-	370	282	288	57	50
$\dot{\gamma}_0$ $[s^{-1}]$ (10^{-3})	4.08	-	3.02	0.56	1.30	0.45	0.39
h_0 [MPa]	203	-	230	268	269	24	19
τ_{sat} [MPa]	482	-	394	378	380	101	98
m	8	-	2.44	3.13	4.191	0.1	0.1
n	0.62	-	0.86	1.61	1.37	0.57	0.50

Table 3. Numerical simulation parameters.

	α	β
τ_0^{avg} [MPa]	Table 2	57.60
$\dot{\gamma}_0^{avg}$ $[s^{-1}]$ (10^{-3})	2.38	0.450
h_0^{avg} [MPa]	220.605	24.570
τ_{sat}^{avg} [MPa]	482.339	101.679
m	4.290	0.1
n	0.785	0.570
c/a	1.59	1

Table 4: Single elastic constant of α and β phase in Ti-6242S at 730°C

	C_{11} [GPa]	C_{12} [GPa]	C_{44} [GPa]	C_{33} [GPa]	C_{13} [GPa]
α	133.9	64.8	40	157.5	46.3
β	129.5	104.8	48.50	-	-

Fig. 6 shows the comparison between the simulation and experimental true stress vs true strain. It can be observed that the result of the simulated material global response well reproduced the experiment material macroscopic true stress vs true strain curve. This shows the accuracy of the obtained model parameters identification and the modelling approach.

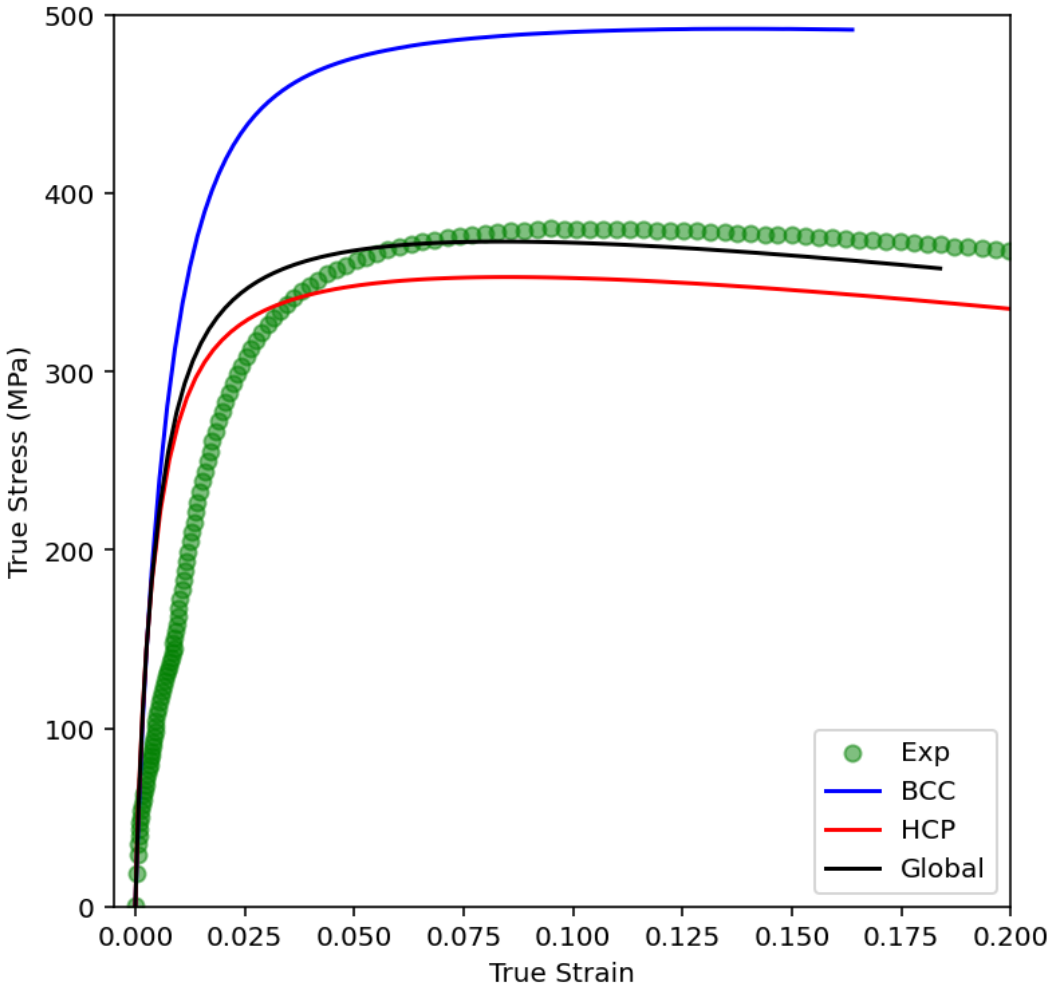

Fig. 6. Comparison of True stress vs true strain from simulation and experiment at 730°C.

Further, the elastic region of simulated results, α and β phase, coincide with the elastic stiffness of the material when local yielding has not started (indicated by the first stiffness, see Fig. 3d). The β phase flow stress is higher than that of the α phase, which means that the β phase is more stressed than the α phase. At a glance at the β phase material properties (Tables 2 and 3) and the equivalent lattice strains (Figs. 5a, b and c), it would be expected that the α phase sustains more stress than the β phase. However, considering that β phase planes has a low critical shearing stress that is about one-tenth of the hardest α phase plane which means that β slip planes are soft and slip activities starts at a low stress (shown in Fig. 5d), which can be seen from the very low value of the equivalent phase lattice strain (Fig. 5c) the β planes begin to shear. All these in addition to the high stiffness of the β phase at 730°C, caused higher stress to be partitioned in β phase than α phase.

In contrast, the lower flow stress in the α phase is due to the fact that the slip shearing can occur at a high stress level due to the hardness of the HCP slip planes. The start of the shearing in β phase at low stress can be considered to be the cause of the reduction in material elastic stiffness reported in Fig. 5c, although this cannot be shown by the simulation result due to the limited number of β grains considered in the RVE compared to the large β grains (probably in millions) in the real sample, and while the continuous increase on a new linear path (second elastic stiffness slope) up to the global plastification of the material can be considered to be the effect of the high α phase fraction (hard slips) on the global material behaviours. The higher stress in the β phase may justify the porosities found inside the β phase and the α/β interfaces/grain boundaries (Fig. 3e), which may reveal the phase interfacial effect in dual-phase material with different hardness of their respective slip planes. This effect is not accounted for here, the modified rule of mixture independently developed by Fan et al. [30], and Ankem and Margolin[31] may be used to quantify this effect.

Conclusion

A multiscale modeling approach was used to simulate the global behaviour of Ti-6242S – using microscale properties of constitutive phases (α + β) identified through the application of a genetic algorithm optimisation method with the microstructural data derived from the advanced HEXRD, coupled with the SEM and EBSD experimental techniques.

It has been shown that from the phase micro-strains (ε^{hkl}) obtained through the HEXRD, the elasto-viscoplastic properties of each constitutive phases of a polycrystalline material can be established and the microstructural phase parameters can be used for multiscale (micro to macroscale) modelling. It was quantitatively established that in a Ti-6242S at 730°C, with f_β 15%, higher stress is partitioned in the β phase than in the α phase. Despite the fact that β phase slip planes are vastly softer (lower initial CRSS) compared to the α phase, whose slip planes have higher initial CRSS. Further, the higher stress in the β phase phase may also have been influenced by the interfacial interaction between the β (softer slips) and the α (harder slips) phase, which caused formation of the observed micro-voids/porosities within β and α/β interfaces (Fig. 5e).

With the HEXRD technique, the real-time anisotropic behaviour of α phase has been shown during mechanical loading, which may have completely gone unnoticed if the technique is not used. Also, through this new one-way model parameters identification technique, the anisotropic effect of the different phase planes can be included in numerical simulation by simply using the appropriate parameters that describes the slip plane in the CPFE simulation.

This methodology will facilitate the quantification of the influences of the different phases in multi-phase material applicable at both low and high temperature investigations. Further improve the understanding of the effect of each constitutive phases in multi-phase materials on the materials global behaviours. This will overall help to adequately design the material optimisation process for effective manufacturing of structures/components. This microstructural model approach is rigorous enough to allow the quantification of the influence of the different phases in polycrystal materials with great accuracy than from the unbounded optimisation approach as earlier noted in [5]. The results have shown that the methodology is a good modelling approach.

References

[1] Nieh TG, Wadsworth J, Sherby OD.: Superplasticity in Metals and Ceramics. Cambridge University Press, Cambridge (1997)

[2] Mosleh, A.O., Kotov, A.D., Vidal, V., Mochugovskiy, A.G., Velay, V., Mikhaylovskaya, A. V.: Initial microstructure influence on Ti–Al–Mo–V alloy's superplastic deformation behavior and deformation mechanisms. Materials Science and Engineering: A. 802, 140626 (2021). https://doi.org/10.1016/J.MSEA.2020.140626

[3] Patankar, S.N., Escobedo, J.P., Field, D.P., Salishchev, G., Galeyev, R.M., Valiakhmetov, O.R., Froes, F.H.: Superior superplastic behavior in fine-grained Ti–6Al–4V sheet. J. Alloys Compd. 345, 221–227 (2002). https://doi.org/10.1016/S0925-8388(02)00406-1

[4] Kolli, R.P., Devaraj, A.: A Review of Metastable Beta Titanium Alloys. Metals (Basel). 8, (2018). https://doi.org/10.3390/met8070506

[5] Alabort, E., Putman, D., Reed, R.C.: Superplasticity in Ti–6Al–4V: Characterisation, modelling and applications. Acta Mater. 95, 428–442 (2015). https://doi.org/10.1016/J.ACTAMAT.2015.04.056

[6] da Silva, L., Sivaswamy, G., Sun, L., Rahimi, S.: Effect of texture and mechanical anisotropy on flow behaviour in Ti–6Al–4V alloy under superplastic forming conditions. Materials Science and Engineering: A. 819, 141367 (2021). https://doi.org/10.1016/J.MSEA.2021.141367

[7] Kapoor, K., Ravi, P., Noraas, R., Park, J.S., Venkatesh, V., Sangid, M.D.: Modeling Ti–6Al–4V using crystal plasticity, calibrated with multi-scale experiments, to understand the effect of the orientation and morphology of the α and β phases on time dependent cyclic loading. J. Mech. Phys. Solids. 146, 104192 (2021). https://doi.org/10.1016/J.JMPS.2020.104192

[8] Roters, F., Eisenlohr, P., Hantcherli, L., Tjahjanto, D.D., Bieler, T.R., Raabe, D.: Overview of constitutive laws, kinematics, homogenization and multiscale methods in crystal plasticity finite-element modeling: Theory, experiments, applications. Acta Mater. 58, 1152–1211 (2010). https://doi.org/10.1016/j.actamat.2009.10.058

[9] Demir, E., Martinez-Pechero, A., Hardie, C., Tarleton, E.: OXFORD-UMAT: An efficient and versatile crystal plasticity framework - ScienceDirect, https://www.sciencedirect.com/science/article/pii/S0020768324004694

[10] Segurado, J., Lebensohn, R.A., Llorca, J.: Computational Homogenization of Polycrystals. Advances in Applied Mechanics. 51, 1–114 (2018). https://doi.org/10.1016/BS.AAMS.2018.07.001

[11] Yonggang Huang: A user-material subroutine incroporating single crystal plasticity in the ABAQUS finite element program. (1991)

[12] Dunne, F.P.E., Rugg, D., Walker, A.: Lengthscale-dependent, elastically anisotropic, physically-based hcp crystal plasticity: Application to cold-dwell fatigue in Ti alloys. Int. J. Plast. 23, 1061–1083 (2007). https://doi.org/10.1016/J.IJPLAS.2006.10.013

[13] Hughes, T.J.R., Winget, J.M.: Finite rotation effects in numerical integration of rate constitutive equations arising in large-deformation analysis. Int. J. Numer. Methods Eng. 15, 1862–1867 (1980)

[14] Waller, I.: Dynamical Theory of Crystal Lattices by M. Born and K. Huang. Acta Crystallogr. 9, 837–838 (1956). https://doi.org/https://doi.org/10.1107/S0365110X56002370

[15] Mouhat, F., Coudert, F.-X.: Necessary and sufficient elastic stability conditions in various crystal systems. Phys. Rev. B. 90, 224104 (2014). https://doi.org/10.1103/PhysRevB.90.224104

[16] Rietveld, H.M.: A profile refinement method for nuclear and magnetic structures. J. Appl. Crystallogr. 2, 65–71 (1969). https://doi.org/10.1107/S0021889869006558

[17] Ashiotis, G., Deschildre, A., Nawaz, Z., Wright, J.P., Karkoulis, D., Picca, F.E., Kieffer, J.: The fast azimuthal integration Python library: pyFAI. J. Appl. Crystallogr. 48, 510–519 (2015). https://doi.org/10.1107/S1600576715004306

[18] Newville, M., Stensitzki, T., Allen, D.B., Ingargiola, A.: LMFIT: Non-Linear Least-Square Minimization and Curve-Fitting for Python, (2014)

[19] Kapoor, K., Ravi, P., Naragani, D., Park, J.S., Almer, J.D., Sangid, M.D.: Strain rate sensitivity, microstructure variations, and stress-assisted β → α″ phase transformation investigation on the mechanical behavior of dual-phase titanium alloys. Mater. Charact. 166, 110410 (2020). https://doi.org/10.1016/J.MATCHAR.2020.110410

[20] Quey, R., Kasemer, M.: The Neper/FEPX Project: Free / Open-source Polycrystal Generation, Deformation Simulation, and Post-processing. IOP Conf. Ser.: Mater. Sci. Eng. 1249, (2022). https://doi.org/10.1088/1757-899X/1249/1/012021

[21] Park, C.H., Lee, B., Semiatin, S.L., Lee, C.S.: Low-temperature superplasticity and coarsening behavior of Ti–6Al–2Sn–4Zr–2Mo–0.1Si. Materials Science and Engineering: A. 527, 5203–5211 (2010). https://doi.org/10.1016/J.MSEA.2010.04.082

[22] Despax, L., Vidal, V., Delagnes, D., Dehmas, M., Matsumoto, H., Velay, V.: Influence of strain rate and temperature on the deformation mechanisms of a fine-grained Ti-6Al-4V alloy. Materials Science and Engineering: A. 790, 139718 (2020). https://doi.org/10.1016/J.MSEA.2020.139718

[23] Ribárik, G., Jóni, B., Ungár, T.: The Convolutional Multiple Whole Profile (CMWP) Fitting Method, a Global Optimization Procedure for Microstructure Determination. Crystals (Basel). (2020)

[24] Ungár, T., Balogh, L., Ribárik, G.: Defect-Related Physical-Profile-Based X-Ray and Neutron Line Profile Analysis. Metallurgical and Materials Transactions A. 41, 1202–1209 (2010). https://doi.org/10.1007/s11661-009-9961-7

[25] Das Bakshi, S., Sinha, D., Ghosh Chowdhury, S.: Anisotropic broadening of XRD peaks of α′-Fe: Williamson-Hall and Warren-Averbach analysis using full width at half maximum (FWHM) and integral breadth (IB). Mater. Charact. 142, 144–153 (2018). https://doi.org/10.1016/J.MATCHAR.2018.05.018

[26] Gong, J., Wilkinson, A.: Investigation of elastic properties of single-crystal α-Ti using microcantilever beams. Philos. Mag. Lett. 90, 503–512 (2010). https://doi.org/10.1080/09500831003772989

[27] Mery, S.H., Villechaise, P., Banerjee, D.: Microplasticity at Room Temperature in a/b Titanium Alloys. Metall Mater Trans A 51. 51, 4931–4969 (2020). https://doi.org/10.1007/s11661-020-05945-4

[28] Kang, J., Oh, H.S., Wei, S., Zhu, G., Nakahata, I., Tasan, C.C.: An in situ study of microstructural strain localization and damage evolution in an (α+β) Ti-Al-V-Fe-Si-O alloy. Acta Mater. 242, 118424 (2023). https://doi.org/10.1016/J.ACTAMAT.2022.118424

[29] Séchepée, I., Dubray, C., Velay, V., Matsumoto, H.: Effects of grain size and β fraction on the deformation modes of a Ti-6Al-2Sn-4Zr-2Mo-Si alloy with equiaxed (α + β) microstructures: Slip trace analysis and multiscale simulation of polycrystal plasticity. J. Alloys Compd. 981, 173722 (2024). https://doi.org/10.1016/J.JALLCOM.2024.173722

[30] Fan, Z., Tsakiropoulos, P., Miodownik, A.P.: A generalized law of mixtures. J. Mater. Sci. 29, 141–150 (1994). https://doi.org/10.1007/BF00356585

[31] Ankem, S., Margolin, H.: A rationalization of stress-strain behavior of two-ductile phase alloys. Metallurgical Transactions A. 17, 2209–2226 (1986). https://doi.org/10.1007/BF02645919